Non-hydrostatic modelling of extreme water levels on Banneg Island, France

Guillaume Dodet, Serge S. Suanez, Fabien Leckler, Fabrice Ardhuin, Bernard Fichaut, Ronan Autret

14^{th} International Workshop on Wave Hindcasting and Forecasting, and 5^{th} Coastal Hazard Symposium
Key West, Florida, USA, Nov 8-13, 2015.

NON-HYDROSTATIC MODELLING OF EXTREME WATER LEVELS ON BANNEG ISLAND, FRANCE

Guillaume Dodet[1], Serge Suanez[1], Fabien Leckler[2], Fabrice Ardhuin[3], Bernard Fichaut[1], Ronan Autret[1]

[1] GEOMER - UMR 6554, CNRS-LETG, Institut Universitaire Européen de la Mer, Plouzané, France, guillaume.dodet@univ-brest.fr, +33 2 98498691

[2] Service Hydrographique et Océanographique de la Marine, Brest, France

[3] Ifremer, Laboratoire de Physique des Océans, UMR 6523, CNRS-Ifremer-UBO-IRD, Brest, France

1 Introduction

Extreme water level events were observed during recent winters on Banneg island [*Ardhuin et al.*, 2011; *Suanez et al.*, 2009], a small island off western Brittany well exposed to the large North Atlantic swells and characterized by steep rocky cliffs on its western part. Based on geomorphic evidences (bedrock scars, overturned boulders, debris lines) and hydrodynamic data, *Fichaut and Suanez* [2011] investigated the quarrying and transport of cliff-top storm deposits induced by giant wave events and partial flooding of the island (Fig.1), while *Suanez et al.* [2009] provided a retrospective analysis of extreme water levels based on a 30-year wave model hindcast and empirical run-up formula.

Later, *Sheremet et al.* [2014] deployed pressure sensor measurements to this site and applied a 1D nonlinear mild-slope model to reveal that the highest water levels could exceed 6.5 m above the astronomical tide during major storms, mainly induced by large infragravity waves. In order to improve our understanding of the storm-induced hydrodynamics in the Iroise sea, a wave buoy was

Figure 1: Left: photograph of the central part of Banneg island in April 1990 after major storms flooded part of the island (credits: Bernard Hallégouët); Right: photograph of the north-western embayment in April 2008. The red shading highlight the blocks that were no longer visible in photographs of April 2014 (credits: Bernard Fichaut).

deployed to the west of Banneg and additional pressure sensors were installed on the western part of the island (Section 2). In addition, a phase-resolving wave model based on the nonlinear shallow water equations, including non-hydrostatic pressure was applied to the study site and the model results were validated against in-situ observations (Section 3). The hydrodynamic data collected during the major storms of February 2014 were analyzed and the model was forced with the hydrodynamic conditions of the morning high tide of February 5, when some of the highest water levels were observed on the island (Section 4). Based on this combined model-data analysis, the incident and infragravity wave dynamics in the nearshore, and the associated sporadic flooding of the island were investigated in the light of previous studies on Banneg island (Section 5).

2 Instrumentation of Banneg Island

Banneg island is located in the Iroise Sea at the north-western edge of the Molene archipelago, between Ouessant island and the tip of western Britanny (Fig.2). This archipelago consists of 18 main vegetalized islands and 111 small islets and reefs totalizing a surface of land of 229 ha lying above highest astronomical tide (ahat) and corresponding to the emerged part of a shallow submerged plateau covering 15.286 ha between 0 and 25 m above mean sea level (amsl). Banneg island is a granite batholith, oriented north-south, 0.8 km long and 0.15 to 0.35 km wide. The western coast is cut into sub-vertical cliffs made up of a series of high headlands (16 m to 20 m above chart datum, acd) with steep slopes ($> 50\%$), and lower (12 m to 13 m acd), less steep cliffs in embayments (15 to 35%). As indicated by *Suanez et al.* [2009] and *Fichaut and Suanez* [2011], these morphological characteristics and evolution of the cliffed west coast are related to the structure and joint system of the bedrock. More than 1000 m^3 of blocks, known as cliff-top storm deposits (CTSD), whose individual weights vary from several kilograms to several tons (up to 30 tons), were quarried from the cliff-top and deposited at the rear of the cliff top edge backing the embayments on a slope that gently dips towards the eastern coast of the island. The furthest inland accumulation is 100 m from the western cliff edge. With an average slope of 4%, the western shoreface decreases down to 70 m depth a few kilometers offshore in the Fromveur Channel.

The Iroise sea is characterized by a semi-diurnal macro-tidal regime with tides ranging from 2.5 m in neap tide conditions to 8.2 m in spring tide conditions. Near Banneg, the maximum tidal range is 8 m, and tidal currents in the Fromveur Channel can reach 4 $m.s^{-1}$ during spring tides. Given its western location, Banneg island is directly affected by North Atlantic ocean swells. However, due to the sheltering effect of Ouessant island, waves reach the island with a W-SW mean direction and with a significant wave height 40% lower than west of Ouessant [*Ardhuin et al.*, 2011]. In addition, *Ardhuin et al.* [2012] showed that the strong tidal currents occuring in the Fromveur Channel have a strong influence on the propagation of incident waves due to current-induced re-

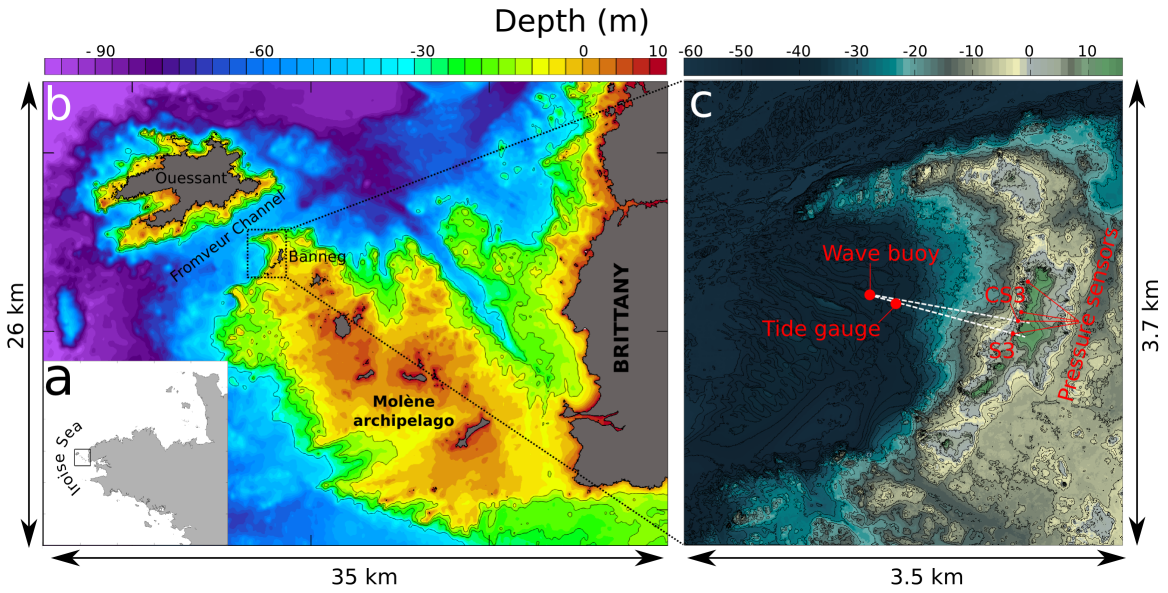

Figure 2: a) Location of the Iroise sea, b) location of Banneg island and bathymetry of Molène archipelago (IGN-SHOM Litto3D data), and c) bathymetry and topography of Banneg island; red circles indicate the positions of the sensors; white dashed lines indicate the SWASH profiles.

fraction, Doppler shifting of frequencies and current-gradient enhanced dissipation.

During winters 2012-2013, 2013-2014 and 2014-2015, several field surveys were carried out at Banneg island to characterize winter hydrodynamic conditions. Every winter, a set of pressure transducers (Ocean Sensor System, OSSI-010-003C) was installed on four embayments of the the western part of the island, along cross-shore profiles (north, centre, south-centre and south) with elevations ranging from 1.5 m below mean sea level (bmsl) to 7.6 amsl (i.e. 3.8 m ahat). The pressure sensors recorded pressure variations continuously at 5Hz during the winter months and were used to compute water levels, wave spectra and mean wave parameters. A cut-off frequency of 0.04Hz was used to compute significant wave height in the incident (>0.04Hz) and ingragravity (<0.04Hz) bands. In addition, a directional waverider (Datawell DWR-MkIII) and a tide gauge (Seabird Electronics SBE26+) were deployed 1.5 km offshore west of Banneg in approximately 50-m water depth in order to measure incident wave parameters and tidal levels.

3 Numerical modelling

3.1 Model description

The SWASH model [Simulating WAves till SHore, *Zijlema et al.*, 2011] is a non-hydrostatic model governed by the non-linear shallow water equations for incompressible fluid with constant density. In a two-dimensional framework, bounded by the free surface $z = \eta(x,t)$ and the bottom $z = -d(x)$, where t is time and x and z are Cartesian coordinates ($z = 0$ is located at the still water level), the governing equations are:

$$\frac{\partial u}{\partial t}+\frac{\partial uu}{\partial x}+\frac{\partial wu}{\partial z}=-\frac{1}{\rho}\frac{\partial(p_h+p_{nh})}{\partial x}+\frac{\partial}{\partial x}\left(\nu^h\frac{\partial u}{\partial x}\right)+\frac{\partial}{\partial z}\left(\nu^v\frac{\partial u}{\partial z}\right) \quad (1)$$

$$\frac{\partial w}{\partial t}+\frac{\partial uw}{\partial x}+\frac{\partial ww}{\partial z}=-\frac{1}{\rho}\frac{\partial(p_h+p_{nh})}{\partial z}+\frac{\partial}{\partial x}\left(\nu^h\frac{\partial w}{\partial x}\right)+\frac{\partial}{\partial z}\left(\nu^v\frac{\partial w}{\partial z}\right)-g \quad (2)$$

$$\frac{\partial u}{\partial x}+\frac{\partial w}{\partial z}=0 \quad (3)$$

where $u(x,z,t)$ is the horizontal velocity, $w(x,z,t)$ is the vertical velocity, ν^h and ν^v are the horizontal and vertical kinematic eddy viscosities, respectively, g is the gravitational acceleration, and p_h and p_{nh} are the hydrostatic and non-hydrostatic pressures, respectively. The hydrostatic pressure is expressed in terms of the free surface as $p_h=\rho g(\eta-z)$ such that $\partial_z p_h=-\rho g$ and $\partial_x p_h=\rho g\partial_x\eta$. An expression for the free surface is obtained by considering the mass balance for the entire water column:

$$\frac{\partial\eta}{\partial t}+\frac{\partial}{\partial x}\int_{-d}^{\eta}udz=0 \quad (4)$$

Kinematic and dynamic boundary conditions are prescribed at the free surface and bottom:

$$w(x,z=\eta,t)=\frac{\partial\eta}{\partial t}+u\frac{\partial\eta}{\partial x} \quad (5)$$

$$w(x,z=-d,t)=_u\frac{\partial d}{\partial x} \quad (6)$$

At the free surface the dynamic boundary condition prescribes a constant pressure ($p_{nh}=p_h=0$) and no surface stresses. At the bottom boundary a bottom stress term is added to the horizontal momentum (Eq. 1). Bottom friction is particularly important for the low-frequency motions since it is one of the mechanisms of energy dissipation. The bottom stress is based on a quadratic friction law $\tau_b=C_f\frac{U|U|}{h}$, where $h=d+\eta$ is the total water depth, C_f is a dimensionless friction coefficient and U is the depth-averaged velocity. In this study we compute the friction coefficient based on the Manning formulation, which reads $C_f=gn/h^{1/3}$ where n is the Manning coefficient. A Manning coefficient of 0.04 $\mathrm{s}^2.\mathrm{m}^{-1/3}$ was chosen to take into account the frictionnal stress induced by the rocky bottom.

3.2 Implementation and validation of the model results

The SWASH model was used in 2DV mode. Two bathymetric profiles were selected (centre-south and south, shown on Fig.2), starting from the location of the waverider, intersecting sensor CS3 and S3 respectively, and ending near the centre of the island. The horizontal mesh resolution was 0.5 m to ensure at least 20 points per wave length for frequencies up to 0.28Hz (i.e. $3\times f_p$, f_p being the lowest peak frequency of the storm cases considered herein). The vertical resolution comprised two layers, which are sufficient to accurately represents dispersion effects for frequencies up to 0.2 Hz [*Zijlema et al.*, 2011]. The western boundary was forced with the wave spectra measured by the waverider and a stationnary mean water level was taken equal to the water levels measured by the tide gauge at the

Table 1: Offshore hydrodynamic conditons used to force the model.

Date	Elevation (m amsl)	Hm0 (m)	Tp (s)	Direction (°)
2014/01/04	3.7	5.0	16.7	264
2014/02/05	3.1	9.0	18.2	262
2014/02/14	3.0	8.4	13.3	238
2014/02/18	2.6	2.5	11.1	270
2015/02/20	3.9	2.9	16.7	267
2015/02/24	2.6	4.1	18.2	264

corresponding date. The time-steps ranged from 0.0015 s to 0.006 s and were limited by a maximum CFL number of 0.5. The durations of the simulations covered 40 minutes and included a 20-min spin-up period. 20-min time series of sea surface elevation sampled at 5Hz were used to estimate wave spectra, mean water level, wave run-up, incident significant wave heigths and infragravity significant wave height.

Six events were selected to compare model results with observations and assess the ability of SWASH to reproduce incident and infragravity waves propagation and transformation in the nearshore. These events correspond to spring tide conditions combined with energetic wave conditions, promoting very high water levels at the island. One event (February 18 2014) with milder wave conditions and average water level was also included in order to assess the model skills in a different context. The wave parameters and water levels recorded by the waverider and the tide gauge, respectively, used as model forcing, are given in Table 1.

The simulated and observed elevation variance density spectra at stations S3 and CS3 are shown on Fig.3, and root-mean-square errors and scatter index of the bulk parameters Hm0, $Hm0_{IG}$, Tm_{02} and Tp are provided in Table 2.

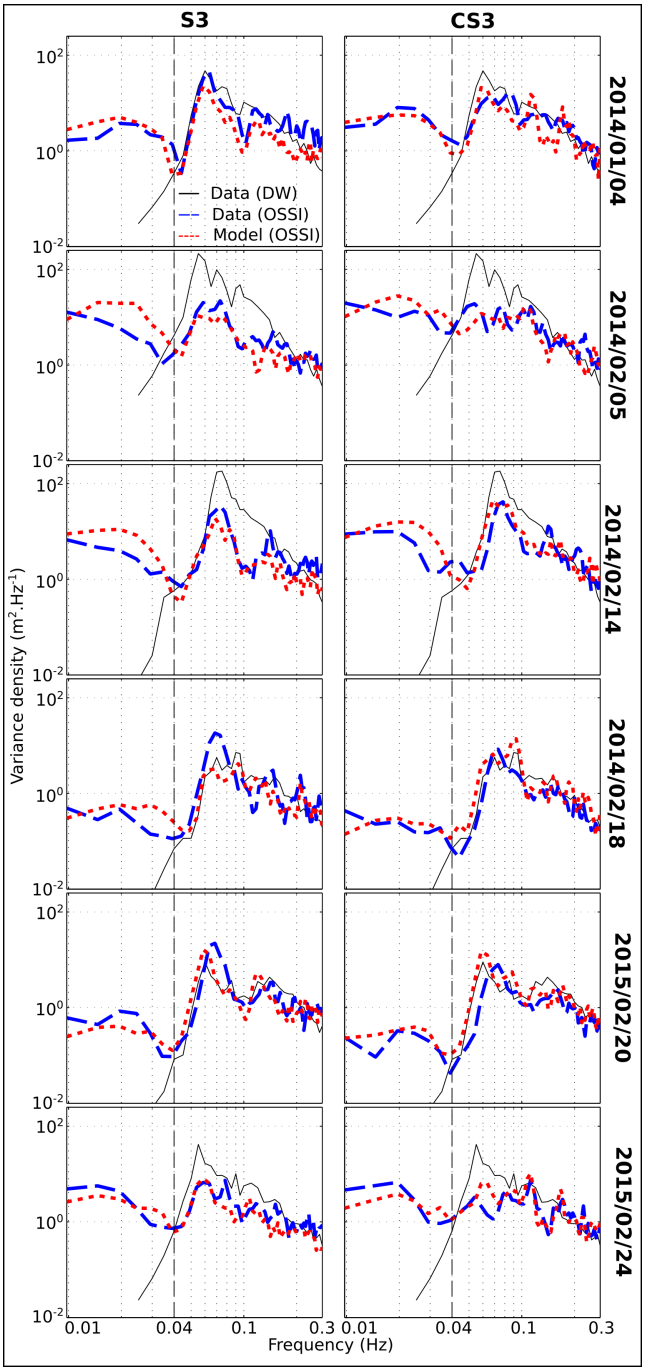

Figure 3: Comparisons between measured (blue line) and modeled (red dashed line) variance density spectra at S3 (left column) and CS3 (right column) for the six selected storms (from top to bottom). The thin black line represents the corresponding waverider spectrum.

Table 2: Scatter index between model results and observed data.

	Hm0 (%)		$Hm0_{IG}$ (%)		Tm02 (%)		Tp (%)	
Sensor	S3	CS3	S3	CS3	S3	CS3	S3	CS3
2014/01/04	30.4	6.7	13.4	6.2	6.3	4.7	8.3	41.7
2014/02/05	18.6	8.6	50.2	21.2	5.2	1.5	36.4	50.0
2014/02/14	25.4	8.6	45.3	30.8	4.8	8.4	7.1	14.3
2014/02/18	28.6	29.5	29.2	1.1	13.6	0.5	26.3	21.1
2015/02/20	10.4	23.1	21.1	16.2	1.1	12.3	16.7	25.0
2015/02/24	12.9	11.0	11.2	16.7	8.2	5.9	33.3	0.1
Average	21.1	14.6	28.4	15.4	6.5	5.6	21.3	25.4

Both the comparisons of modeled and measured spectra, and the scatter index computed for the bulk parameters indicate that the model is able to reproduce rather well the incident energy dissipation and subharmonic energy transfer that occur in shallow water. Unfortunately, only one sensor per profile was underwater for a duration long enough to compute average quantities, and cross-shore variation of the measured wave spectra could not be used to validate the model. Model-data comparisons of water elevation time-series at the highest sensor were carried out though in order to verify that the model results were consistant with observations. An example is shown on Fig.5 for sensor CS1 on February 5 2014.

4 Extreme water levels at Banneg island

4.1 Observations

Over the last three winters, a large number of extreme events in terms of wave height and water levels occured at Banneg island. Major wave events were identified through the combined analysis of the waverider and the pressure sensors data. For the whole period (not shown here), February 2014 clearly stands out with offshore Hm0 exceeding 3 m during 46% of the time and reaching up to 10 m on February 14 (Fig.4). During the same period, sensor S3 recorded incident wave heights up to 5 m and infragravity wave heights up to 2 m (Fig.4). The incident wave height was strongly affected by the tidal modulations of the water level, as evidenced by the semi-diurnal and fornight oscillations. The offshore incident wave height and nearshore infragravity wave height also displayed a weak tidal modulation, slightly asymetric for this latter, as it can be seen in the spectra time-series. Indeed lower and stronger infragravity waves seemed to occur at the beginning of the flood. Extreme water level events at Banneg island were easily detected by the highest pressure sensors, which were only hit by the largest wave up-rushes. During the morning high tide of February 5 2014, sensor N1 which stands 8.5 m acd, measured consecutive wave trains of around 3 m from crest to top (not shown here), indicating a 30-s mean water level 3 m above the observed offshore water level (10.2 m acd). At the same time, the highest sensor CS1,

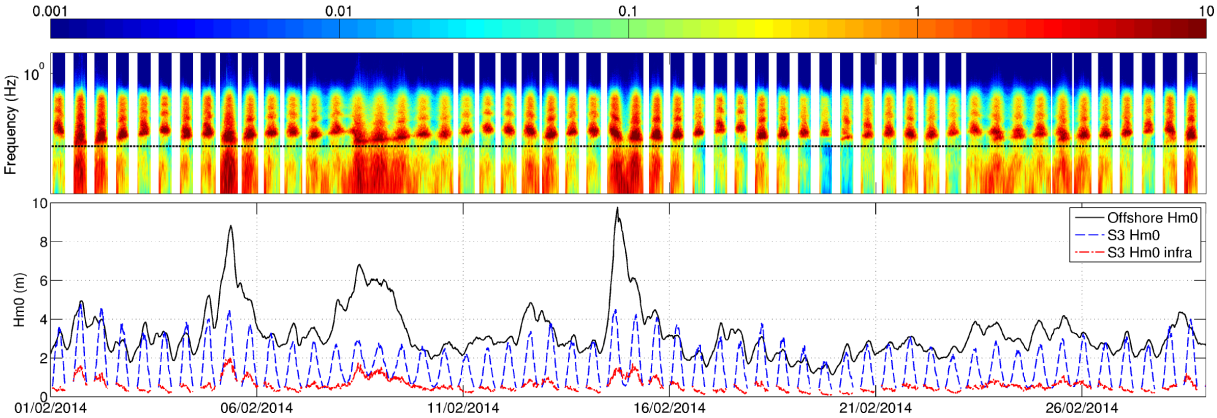

Figure 4: Top panel: time series of wave spectra computed at pressure sensor S3 in February 2014; bottom panel: time series of incident significant wave height measured by the waverider (black line) and pressure sensor S3 (blue dashed line), and infragravity significant wave height at S3 (red dotted line) in February 2014.

which stands at 11.8 m acd (i.e. 3.8 m above the highest astronomical tide), a dozen meters from the top of the cliff and 3.5 m underneath, measured wave crests up to 4 m (Fig.5, upper panel). Such waves are likely to have overwashed the island and quarried large boulders from the cliff top.

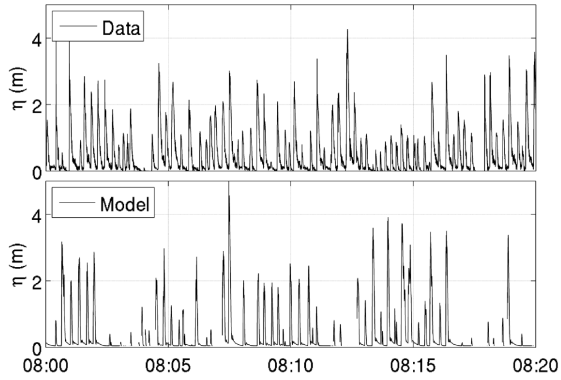

Figure 5: Measured (top panel) and modeled (bottom panel) water surface elevation at pressure sensor CS1 on the morning high tide of February 5 2014.

4.2 Model results

The results of the SWASH model along the centre-south profile during the morning high tide of Feburary 5 2014 brought complementary information on the propagation and dissipation of incident and ingravity waves from the deep water to the shore line. First of all, during the 20-min simulations, several uprushes overwashed the top of the bathymetric profile, indicating a maximum runup larger than 8m (Fig.7, top panel).

The simulated wave spectra at three locations (see Fig.7) along the profile is shown on Fig.6. Comparisons of the spectra reveals minor changes in the gravity band from 25-m depth to 15-m depth and an abrupt decrease from 15-m to 5-m depth. In the infragravity band, energy density increased gradually from 25-m depth to 5-m depth.

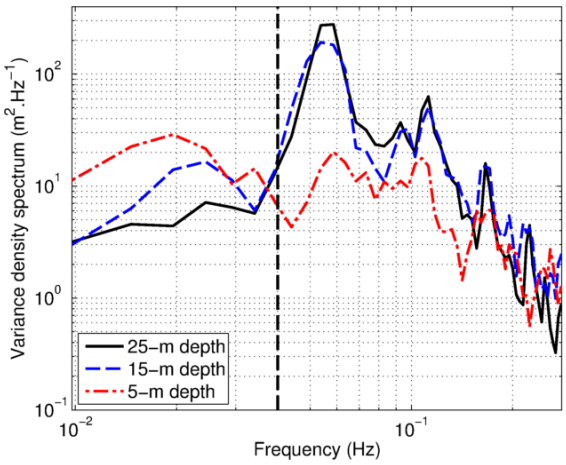

Figure 6: Simulated wave spectra at 25-m depth (black line), 15-m depth (blue dashed line) and 5-m depth (red dashdotted line).

The time-series of mean water elevation (Fig.7, second panel) show a decreasing level from 50-m depth to 10-m depth followed by a rapid increase from 10-m depth to the shore, where the setup rised up to 1 m. The incident wave height (Fig. 7, third panel) is almost constant from offshore to 10-m water depth and decrease rapidly in the shallower region, while the infragrvatiy waves is almost constantly increasing along the whole profile.

5 Discussion and Conclusion

The analysis of the wave data during the last three winters confirmed the unprecedent strength of winter 2013-2014 along the northern Europe coastline, as depicted by several authors [*Castelle et al.*, 2015; *Blaise et al.*, 2015]. Despite its partially sheltered location, Banneg island received very large swells, with maximum Hm0 in 50-m depth reaching 10 m on February 14 (Ulla storm). Both deep- and shallow-water wave signals displayed strong tidal modulation, due to wave-current and wave-bottom interactions, as previously investigated by *Ardhuin et al.* [2012]. The shallow-water infragravity wave height was also tidally modulated and spectral energy displayed a slight asymetry in the infragravity band, which could be induced by current and/or bottom interations.

The episodic overwash events during winter 2013-2014, attested by geomorphic evidences [*Autret et al.*, 2015] were confirmed by model results and measurements at the highest sensors near the top of the cliff. On February 5 2014, the hydrodynamic forcing resulted in a maximum runup larger than 8 m, sufficient to flood part of the island. Using the classical runup formulation empirically derived by *Stockdon et al.* [2006, Eq. 19] with Hm0 and L0 measured this day, the minimum slope to yield a runup higher than 8 m would be 18%, which corresponds to the average slope between the break point (10-m depth) and the upper swash zone (the top of the cliff in this case) in the embayments. Previous studies attempted to calibrate an adequate slope for runup calculation at Banneg island. *Fichaut and Suanez* [2011] used the Mase's formula [*Mase*, 1989] with wave parameters measured west of Ouessant island in 110-m depth and found that shoreface slope values (2%-5%) provided the best runup estimates. However, they obtained almost 100% difference in maximum runup between the northern and southern sectors of the island, due to the strong sensitivity of the Mase's formula with respect to the slope parameter. Also, the offshore wave parameters they used were not representative of the incident waves at Banneg island. *Ardhuin et al.* [2011] used spectral wave model output near the island and correlated it with maximum water levels observed on Banneg island. They found a relation similar to the one of *Stockdon et al.* [2006] with a slope of 8%. With such a slope and the Feburary 5 2014 conditions, Stockdon's formula would predict a maximum runup of 4.5 m, which is too low to overwash the island but might correspond to a local maximum water level in the surf zone.

The analysis of the cross-shore changes of

modeled mean water level and incident wave heights revealed two zones with distinct dynamics (Fig.7, second and third panel). From 50- to 10-m water depth, water level slowly decreases while incident wave height slowly increases. The former effect, known as wave set-down, results from the negative wave radiation stress gradient in the shoaling zone. Further onshore the wave height quickly decreases resulting in a large wave setup (up to 1 m) to balance the positive gradient of wave radiation stress. The cross-shore changes of the infragravity wave height first diplay a slow increase from 50- to 10-m depth and then a steeper increase in the breaking zone. This increase of infragravity wave height in the nearshore is consistent with theory [*Longuet-Higgins and Stewart*, 1962, 1964] and observations [e.g. *Guza and Thornton*, 1985]: shoreward propagating infragravity waves generated by nonlinear interaction between sea-swell waves are amplified in the nearshore zone due to the continuous forcing by the shoaling primary waves and are finally released as free waves when short wave break. In order to complete this analysis, the method proposed by *Sheremet et al.* [2002, Eq.2-4] was used to compute the shoreward and seaward bulk energy fluxes, both in the gravity (Fig.7, fourth panel) and the infragravity (Fig.7, bottom panel) bands. First, these results indicate that incident wave reflection is very weak compared to the infragravity wave reflection. Moreover, the shoreward infragravity fluxes rapidly increase from 30- to 15-m depth, as a result of nonlinear forcing by incident waves, and then decrease in the short wave breaking zone, before being strongly reflected at the shoreline. *Sheremet et al.* [2002] observed similar trends in shoreward infragravity energy fluxes on a gently sloping beach. However, the seaward fluxes they measured were systematically lower than the shoreward fluxes. On the contrary, our case shows seaward fluxes larger than the shoreward fluxes in the deepest part of the profile, corresponding to a R^2 reflection coefficient of 2 and indicating a much stronger infragravity reflection at Banneg island, likely due to the steepness of the bottom profile.

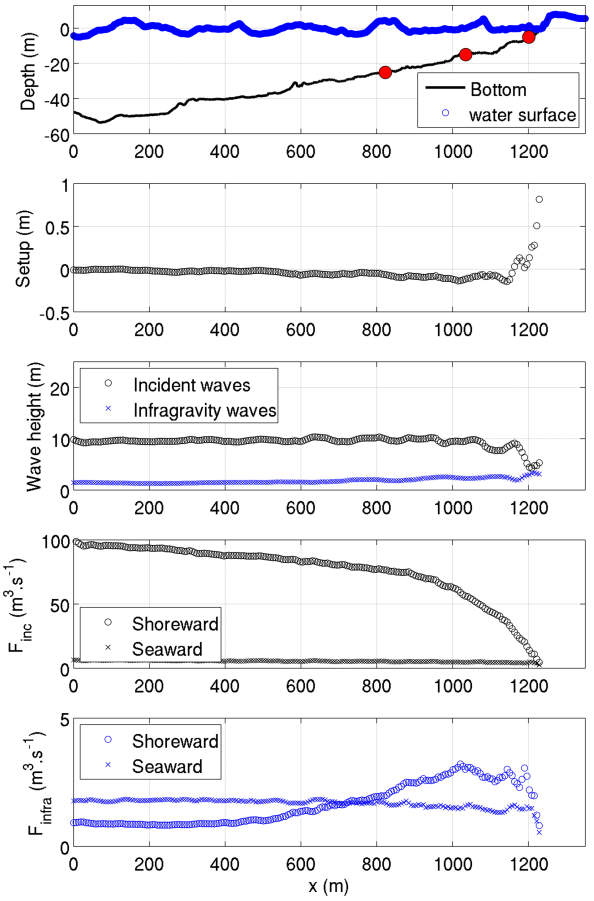

Figure 7: Cross-shore profiles of: modeled water surface elevation at the final time step of the simulation (top panel), and bathymetry (red circles show the selected location for the spectra in Fig.6); 20-min average water surface elevation (second panel); incident (black circles) and infragravity (blue crosses) wave height (third panel), shoreward (circles) and seaward (crosses) bulk incident (fourth panel) and infragravity (fifth panel) energy fluxes.

Acknowlegments

We warmly thank the *Réserve naturelle de la mer d'Iroise* for allowing us to perform the measurements and helping in many ways our access to the site. Many thanks also go to the technical group at the French Navy Hydrographic and Oceanographic Institute (SHOM) who deployed and recovered the instruments. The Litto3D coastal digital elevation model co-produced by IGN and SHOM from numerous Lidar and MBES surveys was of great help in this project. This work is part of the research program PROTEVS (research contract 12CR6) funded by DGA and conducted by SHOM. This work was also supported by the French *Agence Nationale de la Recherche* through the *Laboratoire d'Excellence* LabexMER (ANR-10-LABX-19) program, and co-funded by a grant from the French government through the *Investissements d'Avenir* program.

References

Ardhuin, F., L. Pineau-Guillou, B. Fichaut, S. Suanez, D. Corman, and J.-F. Filipot (2011), Extreme set-up and run-up on steep cliffs (Banneg Island, France), in *12th International Workshop on Wave Hindcasting and Forecasting and 3rd Coastal Hazard Symposium, October 30-November 4, Kohala Coast, Hawaii*, pp. 9–p.

Ardhuin, F., et al. (2012), Numerical Wave Modeling in Conditions with Strong Currents: Dissipation, Refraction, and Relative Wind, *Journal of Physical Oceanography*, *42*(12), 2101–2120, doi:10.1175/JPO-D-11-0220.1.

Autret, R., B. Fichaut, S. Suanez, G. Dodet, L. David, F. Ardhuin, and S. Etienne (2015), Use of airborne methods and hydrodynamic measurements to analyze quarrying and transport of megaclasts, in *Gradualism vs Catastrophism in Landscape Evolution . International conference held in Barnaul, Russia, July 2 - 4, 2015. Extended abstracts*, p. 213, Publishing House of Altai State University, Barnaul, Russia.

Blaise, E., et al. (2015), Bilan des tempêtes de l'hiver 2013-2014 sur la dynamique de recul du trait de côte en Bretagne, *Géomorphologie : relief, processus, environnement*, *21*(3), 267–292, doi:10.4000/geomorphologie.11104.

Castelle, B., V. Marieu, S. Bujan, K. Splinter, A. Robinet, N. Sénéchal, and S. Ferreira (2015), Impact of the winter 2013-2014 series of severe Western Europe storms on a double-barred sandy coast: Beach and dune erosion and megacusp embayments, *Geomorphology*, *238*, 135–148, doi:10.1016/j.geomorph.2015.03.006.

Fichaut, B., and S. Suanez (2011), Quarrying, transport and deposition of cliff-top storm deposits during extreme events: Banneg Island, Brittany, *Marine Geology*, *283*(1–4), 36–55, doi:10.1016/j.margeo.2010.11.003.

Guza, R. T., and E. B. Thornton (1985), Observations of surf beat, *Journal of Geophysical Research: Oceans*, *90*(C2), 3161–3172, doi:10.1029/JC090iC02p03161.

Longuet-Higgins, M., and R. Stewart (1964), Radiation stresses in water waves; a physical discussion, with applications, *Deep Sea Research and Oceanographic Abstracts*, *11*(4), 529–562, doi:10.1016/0011-7471(64)90001-4.

Longuet-Higgins, M. S., and R. W. Stewart (1962), Radiation stress and mass transport in gravity waves, with application to 'surf beats', *Journal of Fluid Mechanics*, *13*(04), 481, doi:10.1017/S0022112062000877.

Mase, H. (1989), Random Wave Runup Height on Gentle Slope, *Journal of Waterway, Port, Coastal, and Ocean Engineering*, *115*(5), 649–661, doi:10.1061/(ASCE)0733-950X(1989)115:5(649).

Sheremet, A., R. T. Guza, S. Elgar, and T. H. C. Herbers (2002), Observations of nearshore infragravity waves: Seaward and shoreward propagating components, *Journal of Geophysical Research: Oceans*, *107*(C8), 10–1, doi:10.1029/2001JC000970.

Sheremet, A., T. Staples, F. Ardhuin, S. Suanez, and B. Fichaut (2014), Observations of large infragravity wave runup at Banneg Island, France, *Geophysical Research Letters*, *41*(3), 976–982, doi:10.1002/2013GL058880.

Stockdon, H. F., R. A. Holman, P. A. Howd, and A. H. Sallenger (2006), Empirical parameterization of setup, swash, and runup, *Coastal Engineering*, *53*(7), 573–588, doi:10.1016/j.coastaleng.2005.12.005.

Suanez, S., B. Fichaut, and R. Magne (2009), Cliff-top storm deposits on Banneg Island, Brittany, France: Effects of giant waves in the Eastern Atlantic Ocean, *Sedimentary Geology*, *220*(1-2), 12–28, doi:10.1016/j.sedgeo.2009.06.004.

Zijlema, M., G. Stelling, and P. Smit (2011), SWASH: An operational public domain code for simulating wave fields and rapidly varied flows in coastal waters, *Coastal Engineering*, *58*(10), 992–1012, doi:10.1016/j.coastaleng.2011.05.015.